Magnetic characterisation of microstructural feature distribution in P9 and T22 steels by major and minor BH loop measurements

Jun Liu [a,*,1], John Wilson [b], Martin Strangwood [a], Claire L. Davis [a,1], Anthony Peyton [b]

[a] School of Metallurgy & Materials, University of Birmingham, Edgbaston, Birmingham B15 2TT, UK
[b] School of Electrical and Electronic Engineering, The University of Manchester, Manchester M13 9PL, UK

ARTICLE INFO

ABSTRACT

This paper investigates the magnetic properties and parameters measured from major/minor loops and used to characterise different microstructural feature distributions in P9 and T22 steel in different heat treatment or service conditions. The present study introduces a non-destructive way of selecting microstructural features of interest and/or excluding those of little relevance by examination of minor loop measurements at a selected range of applied fields and discusses the fundamental mechanism in terms of domain processes. There is remarkable consistency in magnetic behaviours and properties such as initial/incremental permeability values between the measurements by different techniques. This behaviour has been ascribed to the similar underlying domain processes and hence similar selected microstructural features that are affecting the domain processes.

1. Introduction

Microstructural changes in power generation steels during operation at elevated temperature alter the properties of these steels and their remaining safe operating life (remnant life) [1]. Efficient operation of power generation plant requires the microstructural condition to be assessed during service. Currently the microstructural state is assessed using replicas of the surface or inferred from hardness measurements, both taken during shut down periods. Non-destructive evaluation (NDE) of the microstructural state of power plant steels during their service life is of interest in order to give a more accurate assessment of safe remnant life. Amongst a wide range of NDE techniques available, electromagnetic (EM) methods are of particular interest for the evaluation of ferromagnetic ferritic heat resistant steels.

A variety of EM sensors have been developed or commercialised for evaluating/monitoring microstructure, mechanical properties or creep damage in ferritic steels during industrial processing, heat treatment or service exposure [2–4]. These sensors operate in a non-destructive and non-contact fashion and are based on the principle that microstructural changes in ferritic steels alter their electrical and magnetic properties. Typical EM sensor measurements involve applying a magnetic field of given amplitude and direction and measuring the EM responses of the test piece. Ferromagnetic materials such as ferritic steels contain magnetic domains, consisting of aligned magnetic moments, separated by domain walls (DWs). Each magnetic moment has associated with it a certain amount of free energy. The existence of domains is a consequence of energy minimisation. As a magnetic field is applied, domains will be re-aligned through DW motion, domain nucleation and growth, and/or domain rotation until a new minimum free energy state is reached. Microstructural features can influence these domain processes to modify the energy balance and ease of domain re-alignment and hence affect the magnetic properties of ferromagnetic materials. More details on the domain theory and the effects of the microstructure in ferromagnetic materials on their magnetic domains and properties can be found elsewhere [5]. The domain processes and the role of microstructural features are affected by the amplitude, direction (with respect to the crystal orientation of the materials) and nature (e.g. alternating or direct current) of the applied fields during EM measurements, which determines what microstructural features an EM sensor or technique is most sensitive to and what relevant EM properties or signals should be measured. For examples, our multi-frequency EM sensors, that apply a small magnetic field, have been used to measure the initial relative permeability of power generation P9 and T22 steels in different conditions and are sensitive to the microstructural features that determine the mean free path (MFP) to DW motion in a small

* Corresponding author.
E-mail addresses: sam.j.liu@gmail.com, j.liu.2@warwick.ac.uk (J. Liu), john.wilson@manchester.ac.uk (J. Wilson), m.strangwood@bham.ac.uk (M. Strangwood), Claire.Davis@warwick.ac.uk (C.L. Davis), a.peyton@manchester.ac.uk (A. Peyton).
[1] Present address: Advanced Steel Research Centre, Warwick Manufacturing Group, University of Warwick, Coventry CV4 7AL, UK. The underlying data behind this article may be accessed through the corresponding author.

Nomenclature

B	magnetic induction
B_r^m	minor remanence
B_r	remanence
B_s	saturation induction
D	lath size for P9N, P9T and T22T or ferrite grain size in equivalent circular diameter for P9ES and T22ES
H	magnetic field
H_0^m	DC bias field for minor loops
H_a^m	amplitude for minor loops
H_c^m	minor coercivity
H_c	coercivity
N	number density of carbide precipitates
W_h^m	minor hysteresis loss
W_h	hysteresis loss
$\mu_{\Delta max}^{major}$	maximum incremental permeability value for biased minor loop excursions from major loops
$\mu_{\Delta max}^{init}$	maximum incremental permeability value for biased minor loop excursions from initial magnetisation curve
μ_Δ	incremental permeability
μ_i	initial permeability
μ_r	relative permeability
ϕ_A	total area fraction of carbide precipitates
ξ_d	dislocation density
d	mean equivalent diameter of grains
d_{nn}	nearest neighbour spacing for precipitates within ferrite grains
g_h	high angle boundary (>15°) density
g_l	low angle boundary (3–15°) density
$\mu_{\Delta max}$	maximum incremental permeability value for the unbiased minor loops
CDF	cumulative distribution function
DW	domain wall
EM	electromagnetic
MFP	mean free path
NDE	non-destructive evaluation
PDF	probably distribution function

applied field [6]. By contrast, a commercial system (IMPOC) used for strip steel assessment applies a very strong field to bring a selected area on a moving steel strip close to its magnetic saturation and correlates the measured EM signals (related to remanence and/or degree of magnetic saturation) to the yield strength of the test materials [3]. Use of major/minor loop assessment for NDE of steels, such as inspection of cold rolling [7,8], creep [9] and degradation (fatigue) [10] in a range of steels, has gained increasing consideration in recent years. Whilst there has been significant work on empirical relationships between major/minor measurements and mechanical properties such as hardness or experimental observations e.g. cold rolling reduction or creep strain, there have been few reports on detailed correlation between the measured magnetic properties from major/minor loops and complex microstructural features or parameters in terms of their interaction with domain processes for given applied fields. There are no reports on the relationship between microstructural feature distributions, as opposed to a single microstructural parameter e.g. average grain size, and corresponding major/minor loop behaviour in steels.

In this paper, a BH system that is able to apply a field (H) of any selected range of amplitude, within a specified power limit, and measure the applied field H and the induction (B) in a test sample has been used to measure major and minor BH loops for P9 and T22 steels in different conditions. A variety of magnetic properties evaluated from the measured major/minor BH loops have been used to characterise the microstructural feature distribution in the studied steels based on their interaction with the domain processes. The present study introduces a non-destructive way of selecting microstructural features of interest by minor loop measurements at a selected range of applied fields and explains the fundamental mechanism in terms of relevant domain processes.

2. Materials and experimental details

The P9 and T22 steels (P9ES and T22ES) studied were removed from a refinery furnace at a petrochemical plant after approximately 11 years at 793 K (520 °C) (comparable with a similar time of elevated temperature exposure during service in power generation plant [11]). Their chemical compositions are given in Table 1. Selected samples (approx. 70 mm × 15 mm × 7 mm) were heat

Table 1
Chemical composition (wt%) of the P9 and T22 steels studied.

Steel grade	Cr	Mo	C	Si	Mn	P	S
P9	8.40	0.97	0.12	0.52	0.44	0.006	0.010
T22	2.14	1.01	0.15	0.28	0.44	0.017	0.011

treated to simulate the service entry microstructure, i.e. tempered martensite/bainite, by normalizing at 1223 K (950 °C) for 1 h or 1213 K (940 °C) for 1 h followed by air cooling to room temperature and then tempering at 1033 K (760 °C) for 1 h or 993 K (720 °C) for 1.5 h for P9 and T22 respectively (P9T and T22T). As-normalised samples were also examined (P9N and T22N). The heat treatment conditions have been determined as per ASTM standards A335 [12] and A213 [13] as well as literature data [14–17].

Metallographic samples were polished to a 0.25 μm finish and etched (in Kallings [18] for P9 and in 2% nital for T22). A JEOL-7000 Field Emission Gun Scanning Electron Microscope (FEG-SEM) was used to obtain SEM micrographs. Additional metallographic samples were polished to a 1 μm finish followed by several etching–polishing cycles and a final polishing with OPS (Oxide Polishing Silica) for 10 min for electron backscattering diffraction (EBSD) analysis using an Oxford Inca EBSD in a JEOL-7000 FEG-SEM. Lath boundaries and outlines of carbide particles in SEM micrographs were reconstructed as trace features and objects respectively using Image-Pro Plus. Average distances between two neighbouring trace features were taken as lath width and average length of diameters measured at 2° intervals passing through the object's centroid as equivalent diameter of particles.

An in-house system developed at the University of Manchester was used for BH loop measurement. A magnetic field was applied using a silicon-steel U-core with two excitation coils wrapped around the legs and driven by two power amplifiers fed with a low frequency time varying signal. A machined cylindrical sample (4.95 mm diameter and 50 mm long) was fitted into a slot in the core to maximise coupling between core and sample. The axial applied field (H) was measured using a sensitive (0.16 mV/mA mT) Quantum Well Hall sensor, also developed at the University of Manchester. The flux density of the induced field (B) was measured using a 20-turn encircling coil connected to an instrumentation amplifier. A 1 Hz sinusoidal excitation was used for the measurement of the major loops and the minor loops without a

bias field and 9 cycles were recorded and averaged. A 10 Hz sinusoidal excitation was used to generate the minor loops with a bias field. The sample was taken through several major loop cycles before the applied field was held constant at a pre-determined H value and 90 minor loop cycles were recorded and averaged to reduce noise.

3. Microstructures

The microstructure of as-normalised P9 consists of martensite (of a typical lath width at 297 ± 46 nm, which is close to literature values [19]) and bainite ($<15\%$) as shown in Fig. 1(a). There are a high number density of high angle ($>15°$) boundaries including all the martensitic/bainitic colony/packet boundaries and some lath boundaries and a lower density of low angle (3–$15°$) lath boundaries as shown in Fig. 2(a), an inverse pole figure (IPF) map overlaid with a grain boundary map, and Fig. 2(d), a boundary misorientation distribution histogram, for the as-normalised P9.

Subsequent tempering produced a simulated service entry microstructure, i.e. tempered martensite/bainite as shown in Fig. 1 (b) with the majority of the laths measuring around 380 ± 149 nm wide (consistent with previous data [20]) as measured from SEM images. Some areas without clear lath features are present in the SEM images (probably due to non-uniformity in etching) and were not considered in the measurement. Compared to the as-normalised P9, there is a significant decrease in the number density of low angle boundaries as observed from Fig. 2(b) and (d) due to coarsening of the martensitic laths. Many fine alloy carbides are present along the lath boundaries, together with some coarse equiaxed precipitates. The size of the latter is inconsistent with their formation during tempering and so they are more likely to be coarse carbides from the service-exposed condition that failed to dissolve completely and remained from the prior solution heat treatment as shown in Fig. 1(b). However, these carbides are so widely separated that they are expected to have a negligible effect on the overall pinning of DW motion, compared to other fine precipitates. Although reverse magnetic domains can form around them, there are too few for these precipitates to have a significant effect on the EM properties.

After long service exposure, the microstructure showed equiaxed ferrite grains (of 9.6 ± 5.7 μm in equivalent circular diameter) with large carbides distributed within the ferrite grains or on grain boundaries as shown in Fig. 1(c). Compared to the as-tempered P9, very few low angle boundaries remained after the service exposure as can be seen in the inverse pole figure map overlaid with boundaries shown in Fig. 2(c) and the misorientation distribution shown in Fig. 2(d). Most ferrite grain boundaries are high angle boundaries.

Table 2 gives values for dislocation density (estimated from literature values [21–24]), the high angle and low angle boundary density measured by EBSD, martensitic/bainitic lath width or ferrite grain size, and the mean equivalent circular diameter d, number density N and total area fraction of carbide precipitates Φ_A for the P9 and T22 samples in the different conditions. For the service exposed P9 and T22 the precipitates on the grain boundaries are not included as they are expected to play a very minor role in pinning compared to the grain boundaries on which they precipitated. This is because the carbides on grain boundaries are expected to be similar or weaker pinning points than grain boundaries, and, if present on the grain boundaries, do not provide any additional pinning and hence little contribution to relative permeability [6]. Fig. 3 shows the size distribution for the precipitates in the as tempered and the service exposed P9. It clearly shows an overall coarsening (a 133% increase in size) and a significant broadening of the distribution after long-term, elev-
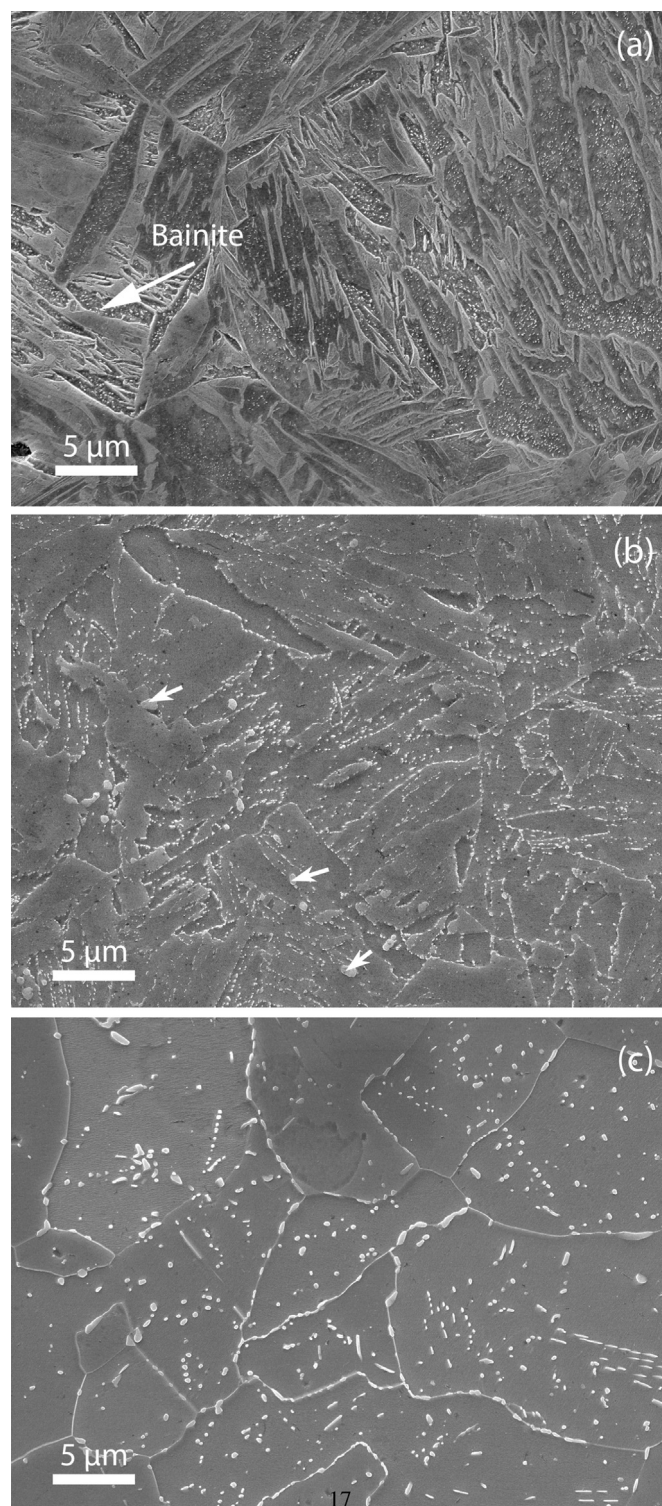

Fig. 1. SEM micrograph of P9 in different conditions: (a) as normalised (b) as normalised and tempered and (c) ex-service. The small white arrows on (b) mark some examples of coarse carbides that failed to dissolve completely during the prior solution heat treatment.

ated temperature exposure in service. The number density of precipitates decreased to only 11% of the as-tempered P9 value accompanied by a 52% reduction in area fraction. Fig. 4 shows the nearest-neighbour inter-particle spacing d_{nn} distribution for the service exposed P9 fitting very well with the log-normal probability distribution function (PDF).
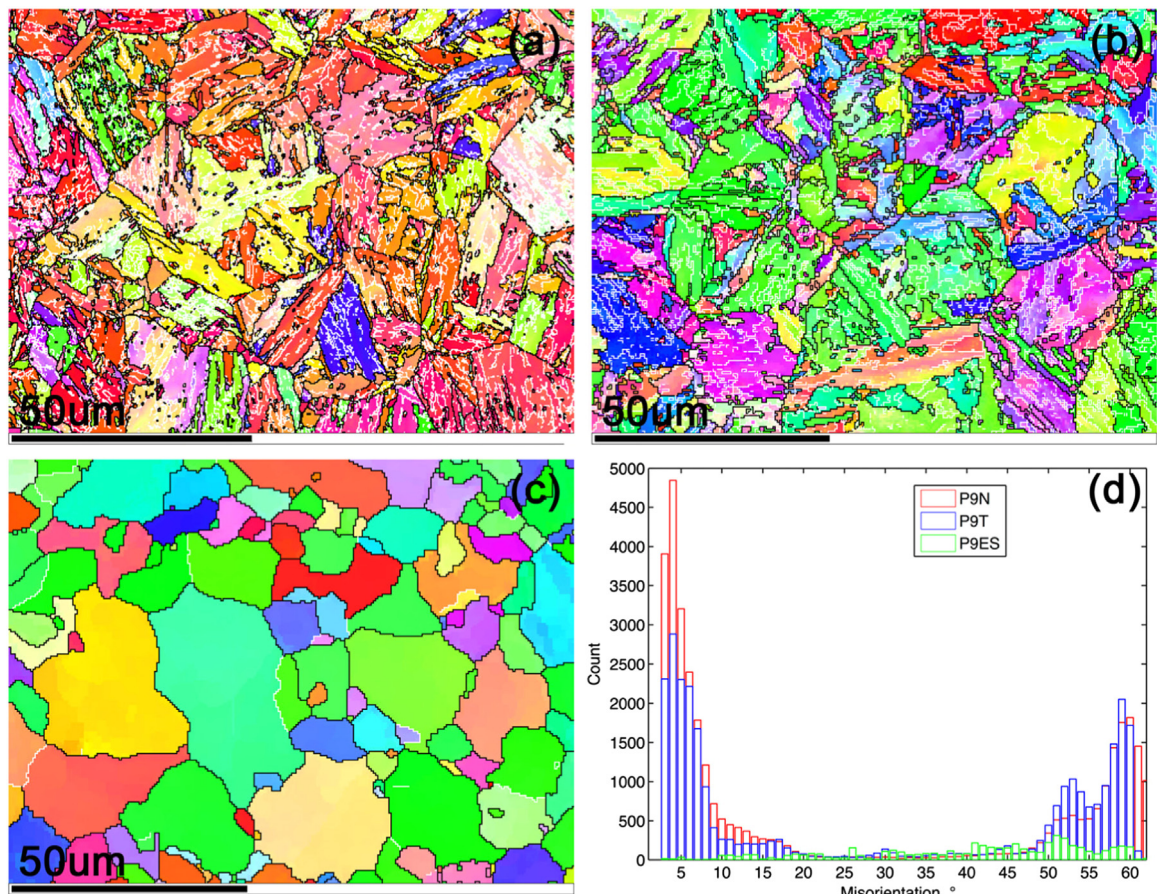
Fig. 2. Inverse pole figure map with low angle (3–15°) and high angle (>15°) boundaries highlighted with white and black line respectively for P9 in different conditions: (a) as normalised, (b) as normalised and tempered and (c) ex-service P9. (d) Distribution of boundary misorientation values. Although some contrast consistent with individual laths is seen in (a) and (b) they are not clearly resolvable at these magnifications and so the features observed are lath packets or lath colonies [6].

Table 2
Measurements on microstructural features for P9 and T22 in different conditions [6].

Sample code[a]	ξ_d[b] $\times 10^{14}$ m^{-2}	g_h[c] $\times 10^5$ m^{-1}	g_l[d] $\times 10^5$ m^{-1}	D[e] (µm)	Carbide precipitates		
					d (nm)	N ($\times 10^{12}$ m^{-2})	Φ_A (%)
P9N	41 [21]	8.56	8.78	0.297 $\pm$ 0.046	–	–	–
P9T	9 [21]	6.47	6.06	0.380 $\pm$ 0.149	105 $\pm$ 61	4.80 $\pm$ 0.24	5.44 $\pm$ 0.5
P9ES	0.06 [22]	2.20	0.16	9.6 $\pm$ 5.7	239 $\pm$ 114	0.55 $\pm$ 0.12	2.74 $\pm$ 0.76
T22N	1.74 [23]	5.30	2.92	–	50 [25]	–	–
T22T	1.27 [23]	5.64	2.53	0.443 $\pm$ 0.136	59 $\pm$ 29	18.36 $\pm$ 0.33	5.79 $\pm$ 0.09
T22ES	0.02 [24]	0.91	0.00	27.5 $\pm$ 17.1	181 $\pm$ 83	1.88 $\pm$ 0.22	5.04 $\pm$ 0.01

[a] Suffixes N as normalised, T as normalised and tempered and ES as ex-service.
[b] ξ_d, Dislocation density. Values are estimated based on literature values for 9Cr–1Mo or 2.25Cr–1Mo steels subject to similar thermal exposure.
[c] g_h, high angle boundary (>15°) density.
[d] g_l, low angle boundary (3–15°) density.
[e] D, lath size for P9N, P9T and T22T or ferrite grain size in equivalent circular diameter for P9ES and T22ES.

The as-normalised T22 steel shows a mixed microstructure of bainite and a small amount (< 5%) of pro-eutectoid ferrite as shown in Fig. 5(a). No carbides are present in the pro-eutectoid ferrite, but plate-like carbides can be seen within the bainitic regions. After tempering, many carbides can be observed along prior austenite grain boundaries, on ferrite boundaries or within bainite regions as shown in Fig. 5(b). The microstructure of T22 after the service exposure consists of equiaxed ferrite grains (27.5 $\pm$ 17.1 µm equivalent circular diameter) and many carbides outlining the ferrite grain boundaries or occurring within the ferrite grains as shown in Fig. 5(c). Fig. 6 shows an inverse pole figure map with highlighted boundaries and a misorientation distribution

histogram for the T22 samples in the different conditions. There is a reduction in the number of low angle boundaries after tempering and a significant decrease in both low and high angle boundaries after the service exposure as a result of annihilation of the ferrite lath boundaries, as can be seen in Fig. 6(d) and Table 2. Fig. 7 compares the extremely fine precipitates within the ferrite laths for the as-tempered T22 and the coarser ones within the ferrite grains for the service exposed T22. Their size distributions are compared in Fig. 8, which shows a similar broadening as seen in Fig. 3 for the P9 samples but a more significant coarsening (182% increase in mean equivalent circular diameter). Fig. 9 shows distributions of the nearest-neighbour inter-particle spacing for the
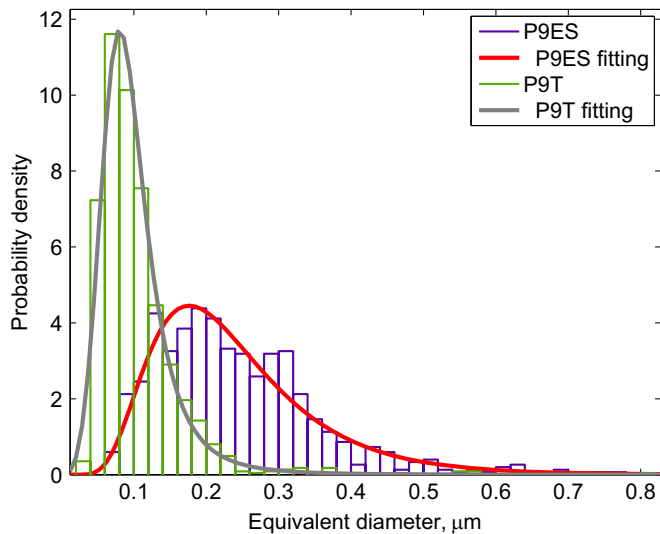
Fig. 3. Size distribution for precipitates in the as-tempered (P9T) and the service exposed (P9ES) P9 samples [6].
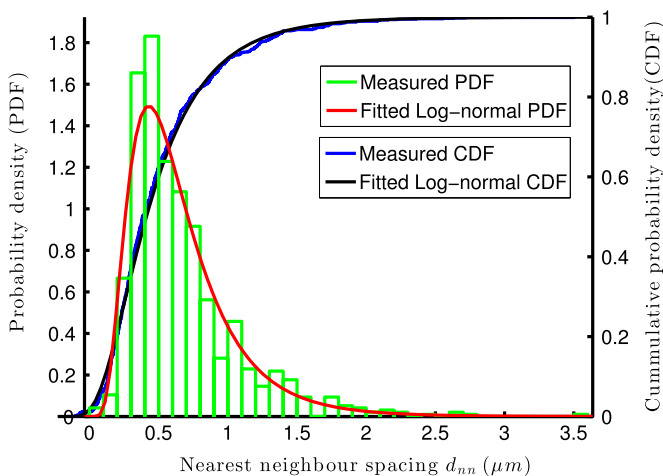

Fig. 4. Distribution of the nearest-neighbour inter-particle spacing for the precipitates within the grains of the service-exposed P9 (P9ES).

intra-grain precipitates in the service-exposed T22 sample also fitting very well with a log-normal PDF and a log-normal cumulative distribution function (CDF).

4. Magnetic measurements

4.1. Major loops

Fig. 10 shows the major BH loops and the initial magnetisation curves for the P9 and T22 steels in the different conditions. A number of micromagnetic properties or parameters extracted from the major loops are illustrated in Fig. 11, including remanence B_r—the remanent induction after the applied field has been removed; coercivity H_c—the field strength required to bring the sample to zero magnetic induction; the maximum induction B_s obtainable under the applied field—an approximation to the technical saturation induction; and the hysteresis loss W_h—represented by the areas encircled by the loops; the values of which are given in Table 3. The coercivity, H_c (also known as magnetic hardness), values for the P9 and the T22 steels dropped by 80% and 66% respectively after tempering, and 40% and 15% further after service exposure. This significant magnetic softening behaviour is
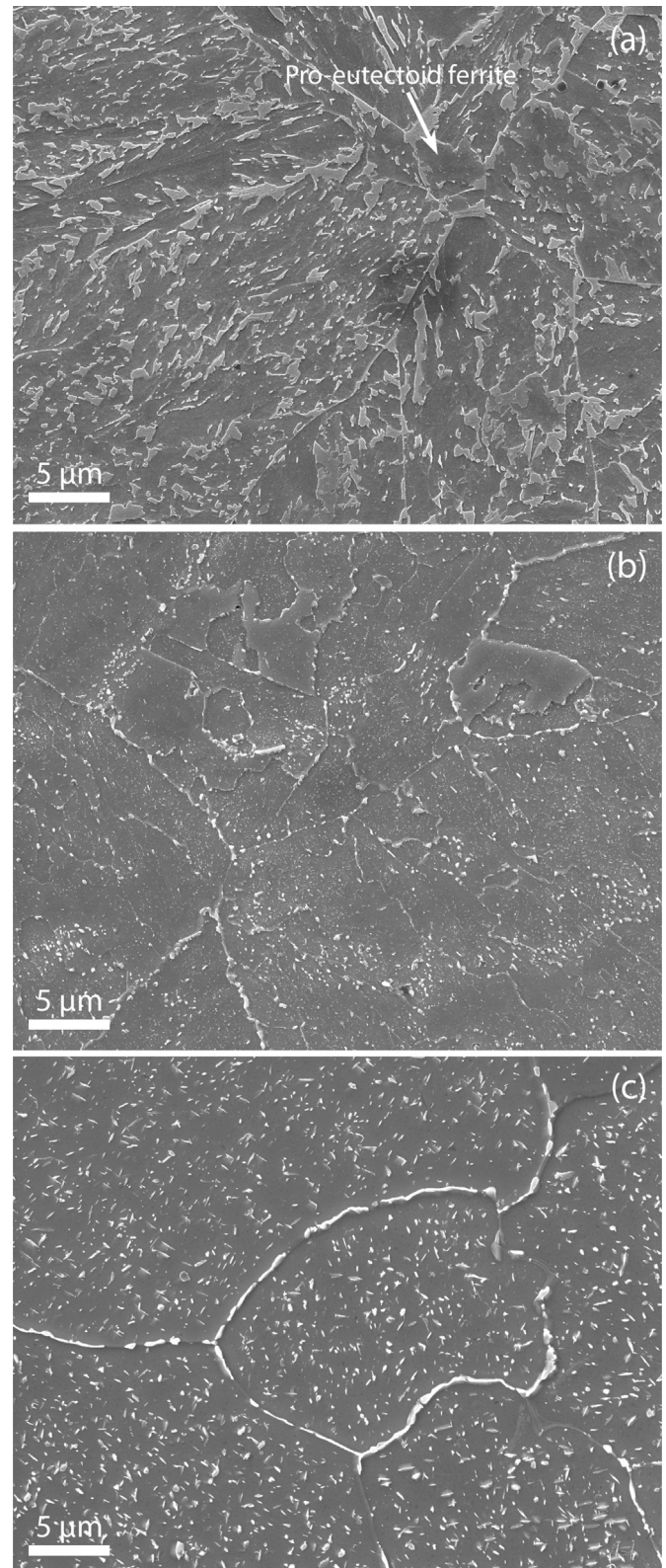

Fig. 5. SEM micrograph for T22 in different conditions: (a) as normalised, (b) as normalised and tempered and (c) ex-service.

consistent with their mechanical hardness decreasing significantly after tempering and service exposure. There is an approximate power-law or cubic relationship between the magnetic and the mechanical hardness for the studied as shown in Fig. 12, which is similar to the reported general trend that coercivity increases with
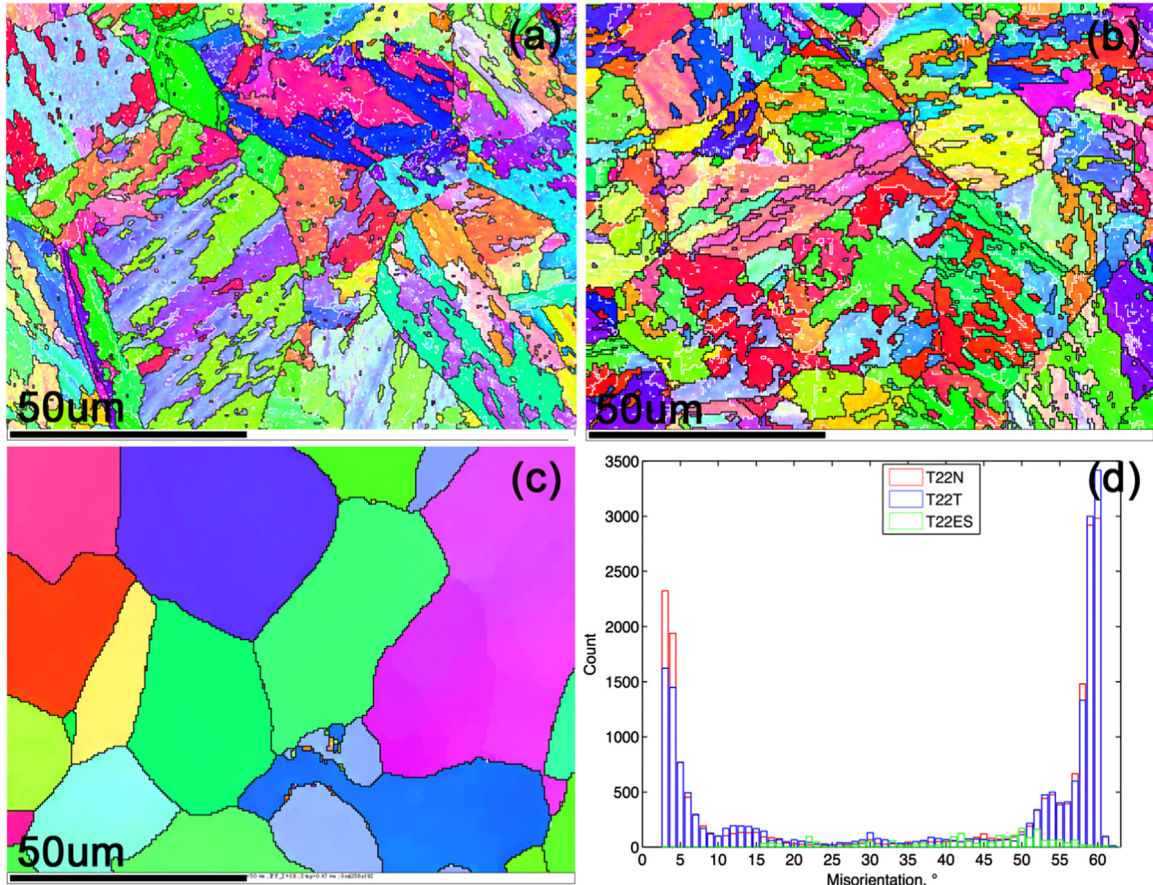
Fig. 6. Inverse pole figure with low angle (3–15°) boundaries highlighted by white line and high angle (> 15°) boundaries by black lines for T22 in different conditions: (a) as normalised, (b) as normalised and tempered and (c) ex-service. (d) Misorientation distribution [6].

hardness [26,27] for different steels and microstructural changes. However, there are no reports of a unanimous form of the relationship that applies for all steels. W_h follows a qualitatively similar trend as H_c for both steels. The order of the values for the other magnetic properties for the different heat treatment or service conditions, however, is different. The B_s for the as-normalised samples for both steels are significantly lower than the as-tempered and the ex-service samples whilst the latter two conditions are hardly distinguishable between each other. The as-tempered samples have the greatest B_r, followed by the normalised and then the ex-service samples, for both steels. In summary the two steels (P9 and T22) exhibit qualitatively the same behaviours for the micromagnetic properties changing with tempering and service exposure except for the order for the $\mu_{\Delta max}$. The reason for this exception is explained in Section 5.2.

4.2. Unbiased minor loops

Fig. 13 shows a series of minor loops with the amplitudes (i.e. $H_a^m/2$) ranging from approximately 100 A/m to 20 kA/m, without a DC bias (i.e. $H_0^m = 0$), taking the P9N sample as an example. The shape of the minor loops evolves from a lenticular shape over the small amplitude range into a sigmoid shape typical of a major loop for ferritic steels with increasing H_a^m. Similar to major loops, a minor loop can be characterised by a set of *minor* micromagnetic properties/parameters defined by analogy with their major loop counterparts, as illustrated in Fig. 11. The shape of the loop can be characterised by minor coercivity H_c^m and minor remanence B_r^m. The energy loss, or minor hysteresis loss W_h^m, is equivalent to the encircled area of the

loop; and the gradient of the loop physically means the incremental permeability μ_Δ for $(H_0^m - H_a^m/2) \leq H \leq (H_0^m + H_a^m/2)$, which is defined as $\mu_\Delta = \Delta B/(\mu_0 H_a^m)$.

Fig. 14 shows these properties as a function of the amplitude, $H_a^m/2$. The incremental permeability values for all the samples increase with the amplitude until reaching a maximum value at a certain amplitude (close to their major coercivity values) and then drop/converge to a small value at high amplitudes (>20 kA/m) as shown in Fig. 14(a), with all the curves fitting perfectly well with a multi-term Gaussian function, i.e. $\mu_\Delta(H_a^m) = \sum_{i=1}^{n} a_i \exp(-\frac{(H_a^m - b_i)^2}{2c_i^2})$, where $4 \leq n \leq 8$, a_i, b_i and c_i are constants independent of H_a^m. The maximum values of the incremental permeability $\mu_{\Delta max}$ (i.e. the peak height) are given in Table 3. As initial permeability μ_i is defined as the differential permeability at zero field, i.e. $\mu_i = \lim_{H_a^m \to 0} \mu_\Delta$, one can approximately evaluate μ_i by extrapolating the μ_Δ results to $H_a^m = 0$. The extrapolated μ_i values prove to be very close to the relative permeability μ_r inferred from the measurements using a multi-frequency EM sensor that uses a very small applied field, results presented elsewhere [4], as described in Table 3. This indicates the unbiased minor loop for a given amplitude describes how a sample magnetically behaves during EM sensor tests using a similar field range and vice versa. Other minor magnetic properties such as B_r^m, H_c^m and W_h^m, as shown in Fig. 14(b), (c) and (d) respectively, in general, exhibit similar behaviours with the increase of the amplitudes, i.e. increasing nearly exponentially over small amplitudes $\lesssim H_c$ (note this part of the curves being nearly linear at double logarithmic scale) and then transitioning to plateauing (for the as-normalised samples) or approaching a
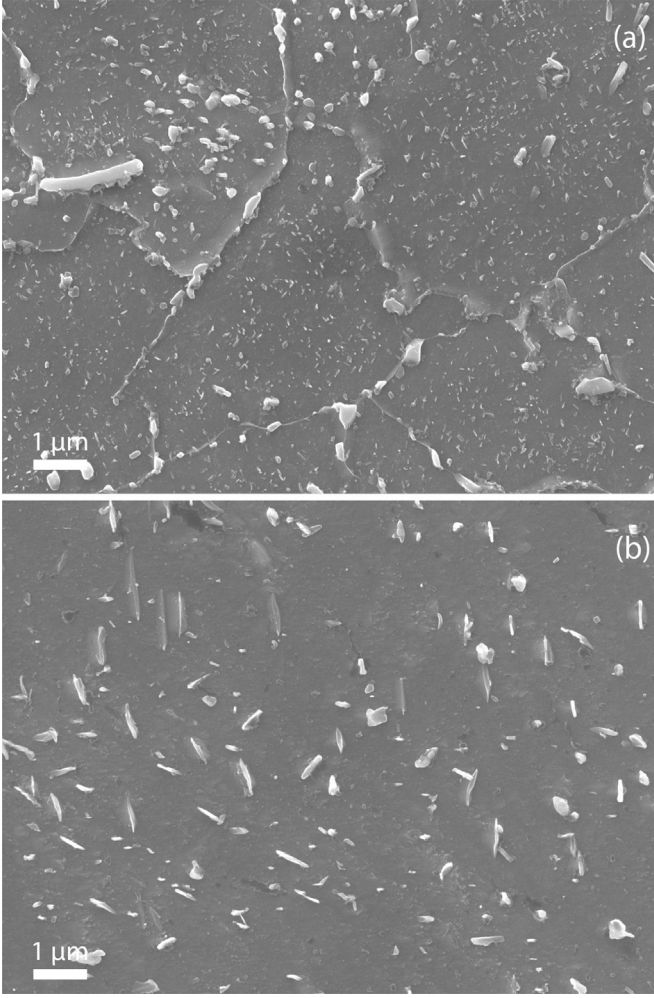
Fig. 7. Precipitates within ferrite laths/grains and at the grain boundaries for (a) the as tempered and (b) the ex-service T22.
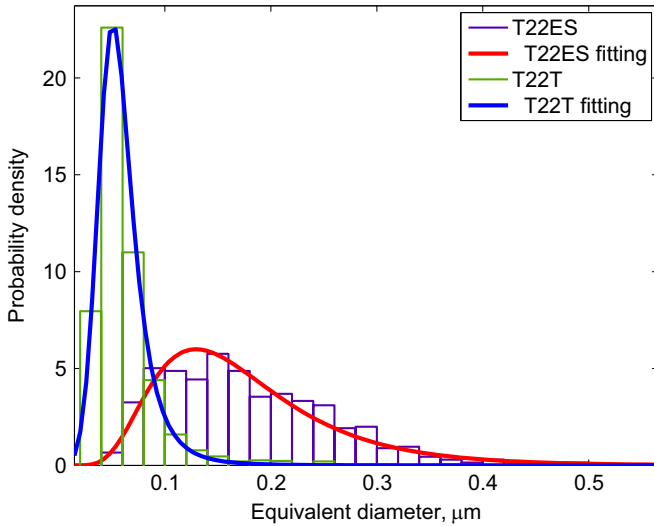

Fig. 8. Size distribution of the precipitates for the as-tempered (T22T) and the service exposed T22 (T22ES) sample [6].

plateau (for the as-tempered and the ex-service samples) at the corresponding major loop values for B_r, H_c or W_h. All the curves, Fig. 14(b)–(d), fit very well with a double exponential function:
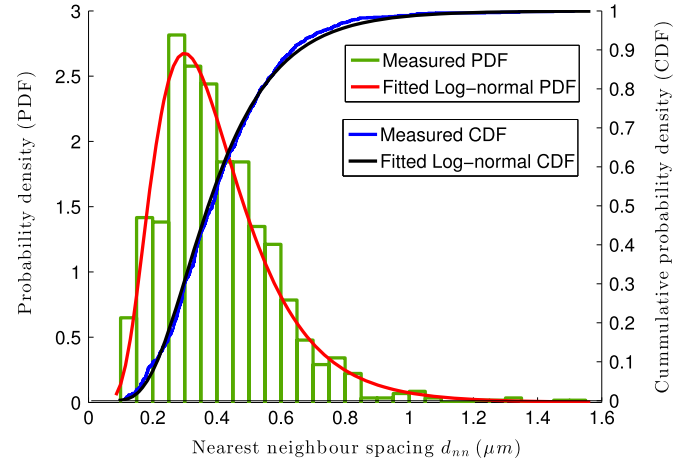

Fig. 9. Distribution of the nearest-neighbour inter-particle spacing for the precipitates within the grains in the ex-service T22 (T22ES) sample.

$y = e^{C_1 \cdot e^{C_2 \cdot x} + C_3 \cdot e^{C_4 \cdot x}}$, where C_1, C_2, C_3 and C_4 are constants independent of the amplitude $H_a^m/2$; the values of which are given in Table 4. It is interesting to note that $C_1^{H_c^m}$ values for both P9 and T22 samples follow a similar trend as the H_c values; $C_2^{H_c^m}$ for the P9 samples are approximately proportional to B_r by a factor of 2×10^{-6}.

4.3. Biased minor loops

4.3.1. Excursion from major loop

Fig. 15 illustrates a series of minor loop excursions from the lower part of the major loop with different DC bias field H_0^m, taking the ex-service P9 sample as an example. It can be seen that the encircled area and gradient of the minor loops vary with H_0^m. Fig. 16 shows the incremental permeability measured from these minor loops, μ_Δ^{major}, as a function of H_0^m for all the studied samples. The μ_Δ^{major} profiles all peak near the corresponding H_c (coercivity for the major loops) and fit perfectly well with a multi-term Gaussian function. The maximum values $\mu_{\Delta_{max}}^{major}$ (i.e. the peak height) are given in Table 3. It is interesting that the $\mu_{\Delta_{max}}^{major}$ values are also close to μ_r. In general the tempering and the service exposure heat treatments, for both steels, significantly increase $\mu_{\Delta_{max}}^{major}$, narrow the peaks and shift them to a lower H_0^m value.

4.3.2. Excursion from initial magnetisation curve

Fig. 17 shows the incremental permeability measured from the minor loop excursions from an initial magnetisation curve, μ_Δ^{init}, with different DC bias field H_0^m ranging from 0 to >15 kA/m for all the studied samples. The μ_Δ^{init} values drop rapidly for $H_0^m \lesssim H_c$ and then decrease at a lower rate with further increase of H_0^m. All the curves fit very well with a multi-term Gaussian function as the incremental permeability profiles for the unbiased minor loops and the biased minor loop excursions from a major loop do. The initial (also the maximum) incremental permeability values, $\mu_{\Delta_{max}}^{init}$, are, in general, close to the relative permeability inferred from the multi-frequency EM sensor measurements, μ_r, the initial permeability extrapolated from incremental permeability for the minor loop amplitude sweep, μ_i, or the maximum incremental permeability for the minor loop excursions from a major loop $\mu_{\Delta_{max}}^{major}$ as described in Table 3. The consistency in the permeability behaviour between different measurements and/or techniques indicates that the underlying domain processes are similar. Note the $\mu_{\Delta_{max}}^{major}$ occurs near H_c, where $B \approx 0$ and the effective field experienced by the domains is comparable with the small field applied for EM sensor measurements for μ_r, the small
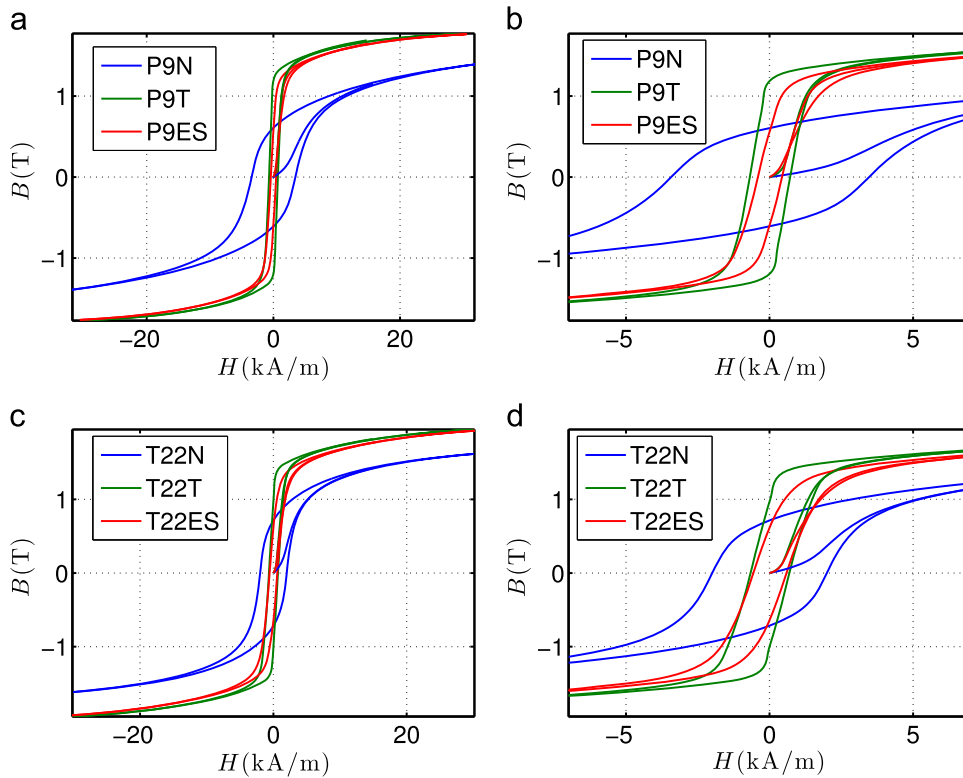
Fig. 10. Major loops and initial magnetisation curves for the P9 samples (a) in full scale and (b) for H between -7 kA/m and 7 kA/m; and for the T22 samples (c) in full scale and (d) for H between -7 kA/m and 7 kA/m.
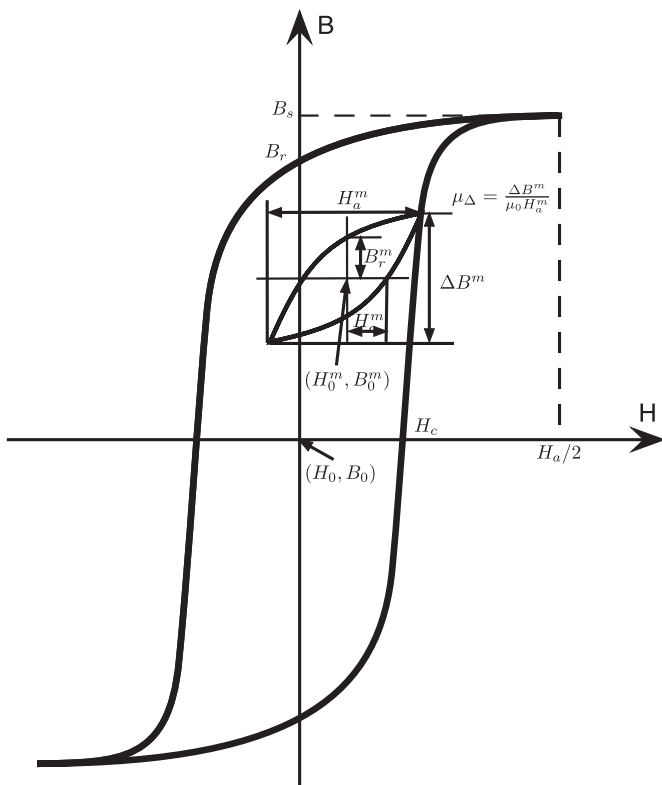

Fig. 11. Illustration of the major/minor loop properties.

amplitude for the unbiased minor loop measurement for μ_i, or the biased minor loop excursion from the initial magnetisation curve at the initial point for the measurement of $\mu_{\Delta max}^{init}$.

5. Discussion

### 5.1. Major loop properties and domain processes

Consider the domain processes during the upper part of a major loop, where the applied field H changes from H_m to $-H_m$. At H_m most of the magnetic dipoles are expected to orientate along the applied field direction so as to minimise the free energy due to the external field (also known as Zeeman energy E_z), forming nearly a single domain across the whole sample. The saturation magnetic induction ($\approx B_s$) is thus determined by the magnetic moments associated with each atoms. Substituting Fe with non-ferromagnetic alloy elements such as Cr and Mo (present in power generation steels such as P9 and T22) reduces the average magnetic moment and hence B_s. This account for the generally lower B_s values for the T22 samples and the lower still for the P9 ones than that of about 2.17 T for pure iron [28]. The significantly lower B_s values for the normalised samples (P9N and T22N) than the as-tempered and the ex-service ones can be attributed to the supersaturated interstitial carbon in solid solution causing lattice distortion and significantly disturbing the coupling between the neighbouring magnetic moments on the lattice. This effect is analogical with interstitial elements e.g. carbon in steels causing more electron diffraction and hence having a more significant effect on residual resistivity in steels than substitutional elements e.g. Cr [29].

As H decreases E_z becomes less competitive, that is, the change in the Zeeman energy, ΔE_z, due to the magnetic moments rotating away from the applied field direction decreases. At the same time the anisotropy energy, E_{an}, due to the deviation of magnetic moments from their easy magnetisation axes becomes a more influential component of the total free energy and hence needs minimising; as a result the magnetic moments rotate towards and eventually align with one of their easy directions associated with

Table 3
Major/minor loop properties for all the studied steels.

Sample	H_c (A/m)	B_r (T)	B_s (T)	W_h (J/m^3)	μ_r [4]	$\mu_{\Delta max}$	μ_i	$\mu_{\Delta max}^{major}$	$\mu_{\Delta max}^{init}$
P9N	3444	0.61	1.39	12,700	37	83	34	37	36
P9T	699	1.19	1.77	4370	66	585	84	79	92
P9ES	421	0.58	1.76	2410	133	656	139	145	138
T22N	1993	0.71	1.62	8730	61	152	60	59	62
T22T	677	0.98	1.95	4700	75	626	78	70	86
T22ES	578	0.63	1.93	3780	86	467	85	89	88
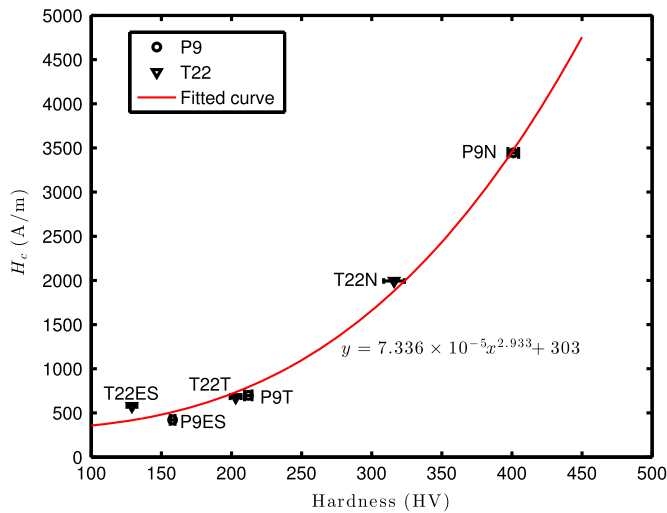
Fig. 12. The coercivity H_c as a function of the Vickers hardness for all the studied samples.
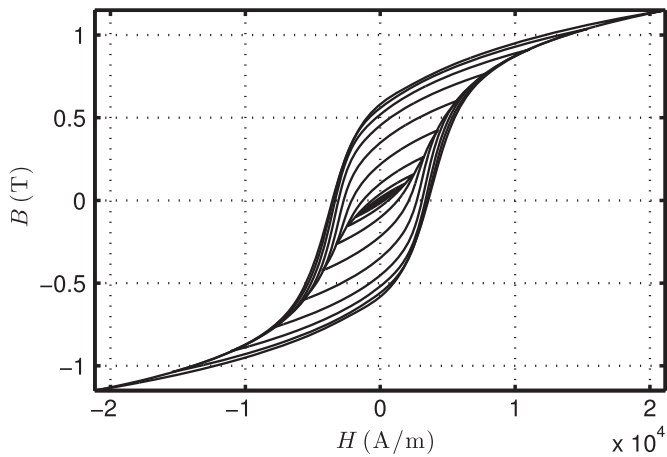
Fig. 13. A series of unbiased minor loops for different amplitude for the P9N sample.

the crystallographic orientations of each grain that is closest to the applied field direction to minimise E_{an}, with a minimum increase in the E_z. It follows that the single domain splits into a number of domains orientated along one of the easy directions closest to the applied field direction, with accommodative DWs formed at grain boundaries. Meanwhile, domains of reverse magnetisation tend to nucleate at the grain boundaries [30] enabling the domain within each grain to split into a group of alternate anti-parallel domains separated by 180° DWs to minimise the demagnetising energy or magneto-static energy, E_d, without affecting E_{an}. As H continues decreasing the growth of the reverse domains, which is against the applied field direction i.e. their direction vector makes an obtuse angle with the direction of H, is favoured at the expense of the

anti-parallel neighbouring domains, accompanied by 180° DW motion until $H=0$. At $H=0$ the 180° DWs are expected to be uniformly spaced provided that there are no imperfections pinning DW motion. Work must be done to overcome the energy barrier for domain nucleation due to the introduction of DW energy. Low-angle boundaries such as martensitic lath boundaries are not energetically favourable nucleation centres for 180° DWs due to the relatively low free magnetic pole density on these boundaries and hence lower driving force for the nucleation. Note $\omega^* = I_s(\cos\theta_1 - \cos\theta_2)$, where I_s is the spontaneous magnetisation, θ_1 and θ_2 the angles between the domain directions of the neighbouring grains and the normal of their common boundaries [30]. It is reported that granular imperfections such as the carbide precipitates within grains do not contribute to the formation of 180° DWs as the critical field required for the nucleation is much larger than the H_c for most soft magnetic materials according to the calculation by Goodenough [30]. Dislocation tangles within the untempered martensite or cold-worked steels can be regarded as point pinning features and hence are expected to have a similar effect as carbide precipitates. However, carbide precipitates within grains may be preferable nucleation centres for closure domains about them so as to minimise the demagnetising energy associated with the magnetic poles present on the surface of the particles so long as their radius is larger than a critical size R_c, which was reported to be approximately 0.1 μm for iron [30]. Most of the precipitates on the lath boundaries in the as-tempered P9 and T22 samples are smaller than R_c, see Figs. 3 and 8. Moreover, they are expected to have relatively low magnetic pole density compared to the equilibrium precipitates occurring within the ferrite grains in the ex-service samples because (a) part of their associated magnetic poles are expected to be counteracted by the lath boundaries intersecting the precipitates; (b) enriching with alloy elements such as Cr, Mo during long service exposure reduces the ferromagnetism of the precipitates and hence increases the density of magnetic poles according to Neel's theory [31]. By contrast, some of the large and equilibrium precipitates observed within the ferrite grains for the ex-service samples (whose diameters are larger than 0.2 μm, Figs. 3 and 8) are possible nucleation centres for closure domains. Thus, the low B_r values for the ex-service samples may be attributed to the formation of closure domains around the large intra-grain carbide precipitates as well as the presence of free poles around the surface of the relatively fine precipitates in the ex-service samples, both promoting the demagnetising process. The low B_r value for the as-normalised samples can be ascribed to the high density of free poles associated with the high density of dislocations within the highly strained martensitic laths providing extra demagnetising energy and promoting the demagnetising process. Meanwhile these microstructural imperfections including the martensitic lath boundaries with precipitates present on them in the as-tempered samples, the dislocation tangles within the laths in the as-normalised samples as well as the precipitates within the ferrite grains in the ex-service samples can be effective pinning features to the 180° DWs and leave them still non-uniformly spaced, with those
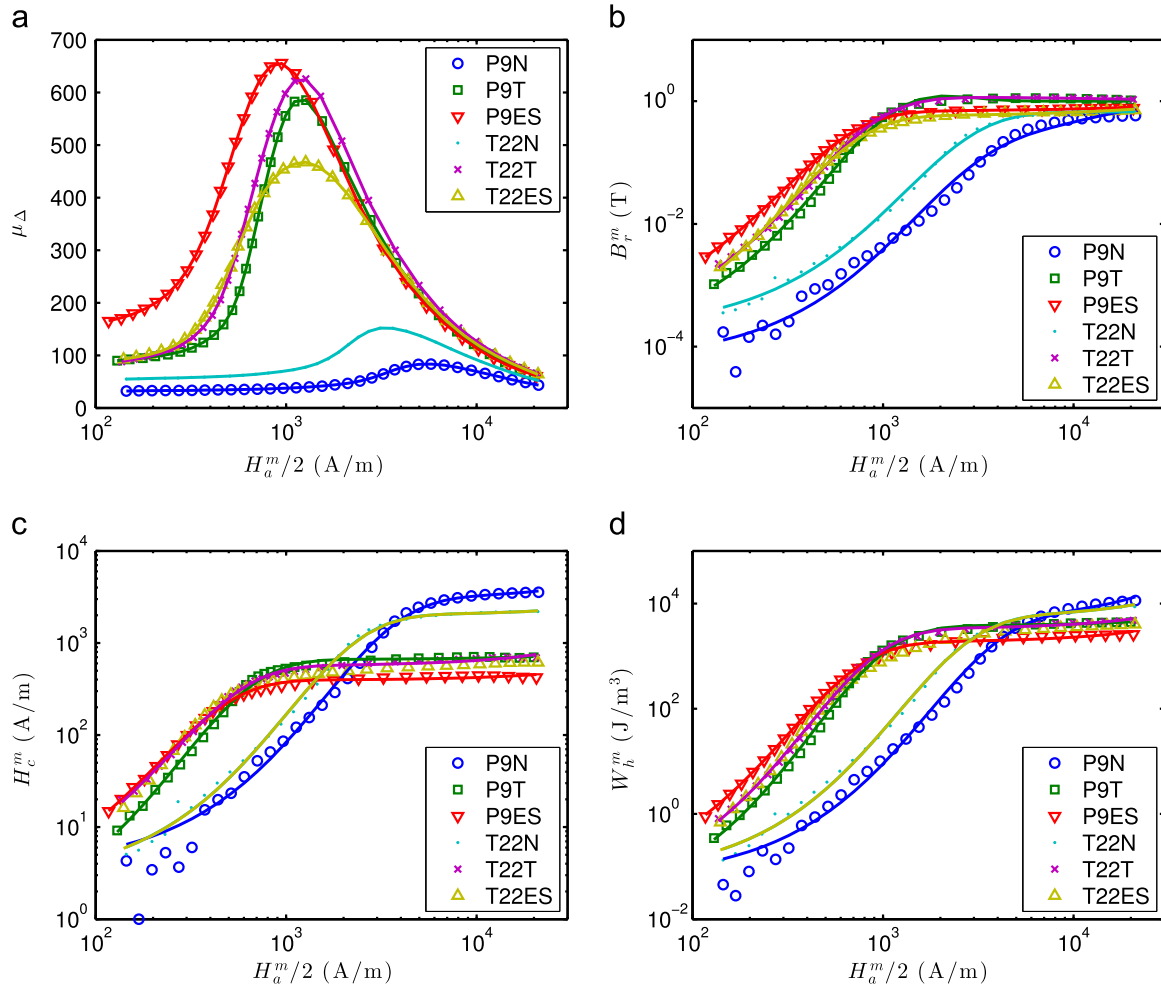
Fig. 14. Minor micromagnetic properties (a) μ_Δ, (b) B_r^m, (c) H_c^m and (d) $W_h^{\prime m}$ as a function of the amplitude for all the studied samples. The fitted curves are shown as solid lines.

Table 4
Fitted constants for the minor coercivity of the amplitude-sweep minor loops.

Parameter	P9N	P9T	P9ES	T22N	T22T	T22ES
$C_1^{H_c^m}$	8.00	6.49	5.98	7.60	6.33	6.15
$C_2^{H_c^m}$ ($\times 10^{-6}$)	1.22	0.57	1.16	0.70	2.16	2.81
$C_3^{H_c^m}$	−6.72	−6.86	−5.66	−6.70	−5.86	−6.58
$C_4^{H_c^m}$ ($\times 10^{-4}$)	−6.28	−35.73	−46.88	−9.92	39.48	−47.92

oriented against the applied field direction being narrower than their anti-parallel neighbours, when H decreases to 0. In other words 180° DWs can be trapped by the potential well associated with these pinning features. Extra driving force is needed to allow further 180° DW movements.

Then, as H is reversed and increases in magnitude the 180° DWs that were originally pinned will eventually overcome the pinning with the narrower parallel domains growing until uniformly spaced, where the B value returns to 0 at H_c. The significant drop in H_c values for both steels after tempering can be attributed to the recovery of the dislocations, coarsening of the martensitic or bainitic laths; and the further drop after service exposure can be attributed to the coarsening of the precipitates and the lath boundaries. These microstructural changes reduce the number density of the pinning features to DW motion and hence H_c. The parallel domains within each grain, which are oriented in favour of the applied field direction, grow at the expense of their anti-

parallel neighbours to minimise the Zeeman energy E_z without affecting the anisotropy energy E_{an} with a further increase in the magnitude of H. This domain process results in a rapid increase in the B value. As E_z becomes more and more competitive with the increase of H and eventually *overthrows* the dominance of E_{an} domains start rotating away from their easy directions towards the applied field direction with the increase of B values slowing down, or the decrease of the differential permeability, and eventually B plateauing at approximately B_s.

5.2. Unbiased minor loop properties

The domain processes during an unbiased minor loop vary with amplitude H_a^m. For small H_a^m 180° DWs oscillating between the microstructural features that are effectively pinning them (i.e. their pinning strength, $f_{pin} > H_a^m$) are predominant domain processes. The spacing between the effective pinning features determines the MFP to DW motion, λ_m, and hence the incremental permeability for a given H_a^m. The microstructural features with $f_{pin} \leq H_a^m$ will be passed through by the DWs and hence have no influence on λ_m. Incremental permeability μ_Δ is determined by the rate of the change of λ_m with respect to H_a^m according to its definition. For a given amplitude increment ΔH_a^m, $\Delta \lambda_m$ (the λ_m increment) is expected to be proportional to the number of the de-pinned ($H_a^m < f_{pin} < H_a^m + \Delta H_a^m$) microstructural features (affecting how many domain walls are moving) as well as the spacing between the original and the new pinning features (affecting how much change in B each movement can make). The latter two
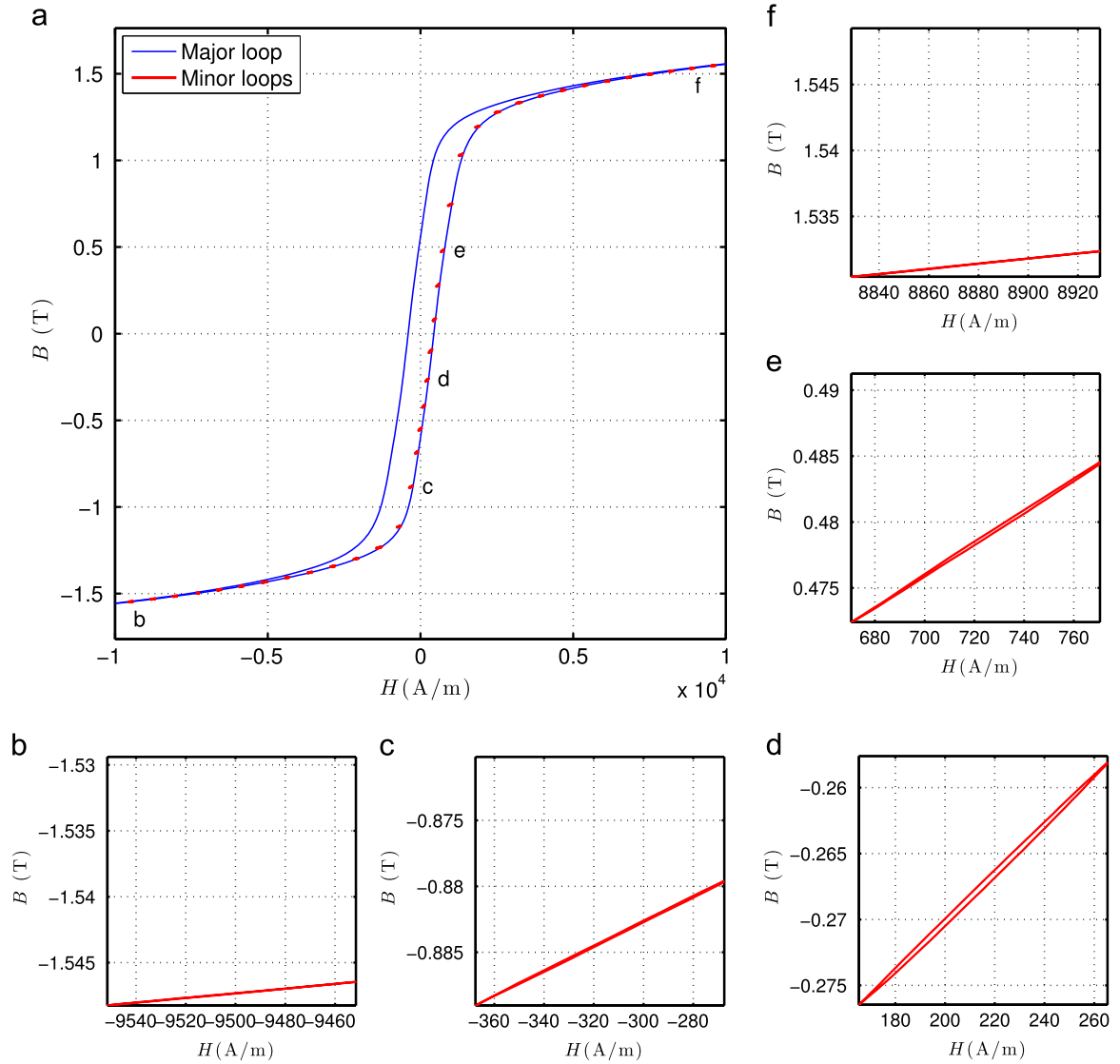
Fig. 15. A series of minor loops excursions from the lower half of the major loop for the P9ES sample as an example. All the minor loops figures have same scales.
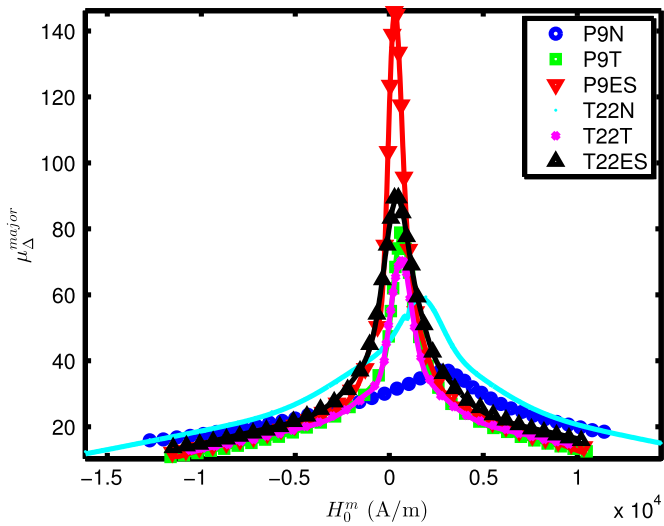

Fig. 16. Incremental permeability for the biased minor loops as a function of the DC bias field H_0^m and fitting with a multiple-term Gaussian function (solid lines).
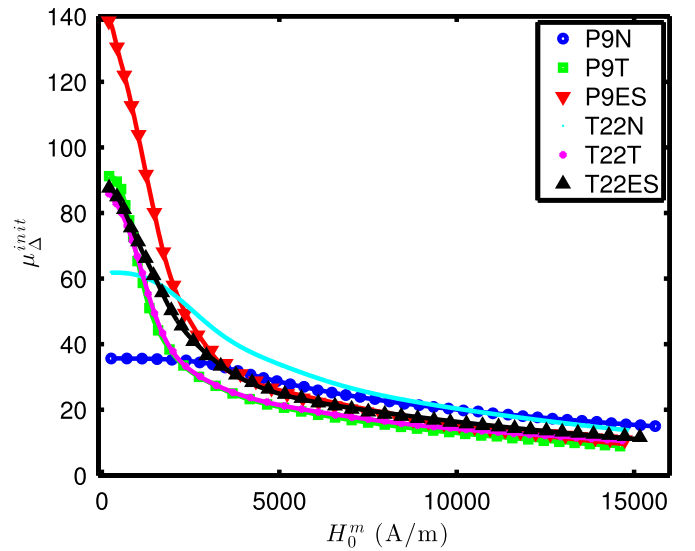

Fig. 17. Incremental permeability for the biased minor loop excursions from the initial magnetisation curve as a function of the DC bias field H_0^m and fitting with a multi-term Gaussian function (solid lines).

parameters are influenced by the probability distribution of f_{pin} as well as the spatial distribution between the pinning features. Thus, it is expected that the probability distribution of f_{pin} will have a similar shape to the incremental permeability profiles shown in Fig. 14(a). It is worth clarifying that f_{pin} in this paper is defined as the minimum applied field H required to enable a domain wall to just overcome the pinning of a microstructural feature. Driving force or ΔE_z, provided by the applied field, is required to overcome two terms of free energy (a) ΔE_d to give a domain wall potential to move and (b) the domain wall energy change due to intersecting the pinning features to enable de-pinning. ΔE_d is influenced by the number density of domains, which is in turn affected by a number of microstructural parameters such as grain size, dislocation density, number density or interparticle spacing of precipitates; DW energy change is influenced by the DW thickness and the size of the pinning feature. It follows that one can characterise the microstructural feature distribution by correlating it with f_{pin} distribution.

The broad μ_Δ profile of the as-normalised P9 sample (P9N) indicates a broad distribution of f_{pin} (with a lower and wide peak), which in turn is associated with an expectedly broad spatial distribution of pinning features including intra-lath dislocation tangles and martensitic lath boundaries (made of dislocation networks). The peak occurring at a higher H value is due to a high number density of dislocations increasing ΔE_d and hence f_{pin}. The peak for the as-tempered P9 (P9T) narrowing and shifting to a lower H value is expected of the recovery of dislocations within the martensitic laths and coarsening of the laths. These microstructural changes narrow the spatial distribution of the pinning features, which become predominantly tempered martensitic laths, as compared to dislocation tangles and untempered martensitic laths for the P9N sample, and increase the mode of the distribution, during tempering. These changes in the microstructural feature distribution alter the corresponding f_{pin} distribution and hence the μ_Δ profile. Further increase in $\mu_{\Delta max}$ for the ex-service sample indicates a narrower f_{pin} distribution due to the coarsening of the martensitic laths into ferrite grains with coarsened precipitates present within the ferrite grains increasing the spacing between the pinning features (i.e. the inter-particle spacing for the intra-grain precipitates compared to martensitic lath width for the as tempered sample). Further shifting to the left after service exposure can be attributed to a significantly reduced area fraction of the precipitates (Table 2) and increased interparticle spacing (see Fig. 4) compared to the lath width (Table 2), which decreases ΔE_d and the number density of domains, shifting the f_{pin} distribution to a lower H value. The as-normalised and as-tempered T22 samples follow the same trend as the P9 counterparts. The lower $\mu_{\Delta max}$ of the ex-service T22 indicates a broader distribution of the inter-particle spacing for the precipitates within the ferrite grains in the T22ES samples compared to that of the bainitic laths in the T22T sample. This can be attributed to the coarsening of the very fine precipitates within the bainitic laths, which were not effective pinning features to DWs [6], into larger and less magnetic precipitates that can pin domain walls altering the f_{pin} distribution. The similar peak position is probably due to a similar area fraction of precipitates (Table 2) and comparable spacing between the pinning features i.e. mode value of inter-particle spacing distribution (Fig. 9) and the lath width (Table 2).

For $H_a^m > H_c$ many pinning features are passed through by the DWs. The 180° DWs may also be annihilated as a result of merging of the antiparallel domains and domains will start to rotate away from the easy direction and towards the applied field direction. The pinning forces, from the high-angle boundaries such as many ferrite grain boundaries or martensitic packet boundaries, are expected to be overcome and the incremental permeability decreases with the increase of H_a^m. Whilst the microstructural

features that are passed through by the DWs have no influence on the incremental permeability they do collectively affect other minor properties including W_h^m, H_c^m and B_r^m. That is, these properties indicate the cumulative distribution of pinning strength of the pinning features, which can then be correlated to the cumulative distribution of microstructural parameters. For example, the size of the precipitates within the ex-service P9 and T22 samples affects the energy loss during domain wall passing through the precipitates and hence can be correlated with W_h^m and similarly H_c^m and B_r^m. The cumulative distribution of the precipitate size for both the ex-service P9 and T22 exhibit a double exponential form, which is consistent with the minor properties including W_h^m, H_c^m and B_r^m as a function of H_a^m fitting well with a double exponential function.

5.3. Biased minor loop properties

The domain processes during a biased minor loop vary with more variables than unbiased ones including the position of excursion i.e. bias field H_0^m, the pre-excursion magnetisation history (e.g. lower/upper part of major loop or initial magnetisation curve) and amplitude H_a^m. An unbiased minor loop can be regarded as a special case with a predetermined excursion position, i.e. the initial magnetisation curve, and a biased field same as the amplitude. For small amplitudes the bias field H_0^m plays a predominant role in the domain processes during a minor loop as it predetermines the domain structure and the involved microstructural features. Under the action of H_0^m the microstructural features with $f_{pin} < |H_0^m|$ will have been passed through by domain walls before excursion and only those with $f_{pin} > |H_0^m|$ effectively influence the domain structure at the point of excursion. Further domain processes during a minor loop with a small amplitude are based on this starting domain structure. These domain processes may include, for example, 180° DWs oscillating by a small amplitude within grains or between precipitates if the DWs are thought to be rigid, or the DWs bowing further or relaxing while being pinned by grain boundaries or precipitates if the DWs are thought to be flexible. Some of the de-pinned features under the action of a bias field, the number of which depends on the amplitude and the f_{pin} distribution around the bias field, may be re-activated to interact with DWs and cause minor hysteresis and hence affect H_c^m, B_c^r and W_h^m. For small amplitude (e.g. much smaller than the coercivity) the majority of the microstructural features with $f_{pin} < |H_0^m|$ have no influence on the domain processes throughout the minor loop and hence will not affect the minor magnetic properties. These important behaviours make it possible to utilise this technique to separate out the microstructural features that are not of interest by applying a bias field H_0^m and at the same time to only examine the remaining *active* features by looking at the μ_Δ^{major} for a small amplitude. One can think of this approach as approximating the initial permeability by applying a small field to a sample at a fully demagnetised initial state with a microstructure consisting of only the selected features (by the bias field) and a static domain structure the same as the one at the starting point of the minor loop. Among the selected features for a certain bias field it is also possible to narrow the selection by varying the amplitude and looking at the minor properties due to irreversible domain processes that cause hysteresis including W_h^m, H_c^m and B_r^m.

For all the biased minor loops measured in this paper the same and very small amplitude was used. Thus, only a small number of microstructural features are involved in irreversible domain processes, which account for the generally small encircled area of the minor loops shown in Fig. 15. The microstructural features that are still effectively pinning domain walls are those with $f_{pin} > |H_0^m|$. One can qualitatively correlate the f_{pin} distribution to, for instance,
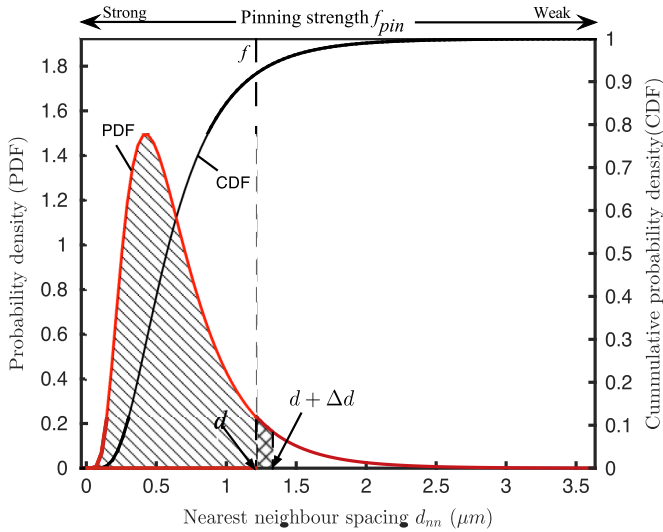
Fig. 18. Illustration of separating microstructural features e.g. precipitates by biased minor loop measurement. Solid lines show an example of probability distribution function and cumulative distribution function profiles for the nearest neighbour spacing of precipitates. The values are for illustration purpose only.

the nearest neighbour spacing distribution of the precipitates within the ferrite grains for the ex-service P9 or T22 samples as these precipitates are predominant pinning features to DWs before domains start rotating away from the easy direction towards the applied field direction. The wider the spacing, the smaller f_{pin} is expected to be as illustrated in [32]. Fig. 18 illustrates a qualitative mapping of f_{pin} to the nearest neighbour spacing distribution. For a given bias field at f the precipitates with a nearest neighbour spacing $d_{nn} < d$ are expected to be effective pinning features and the number of these precipitates can be characterised by the *CDF* (d). The MFP and hence the $\mu_{\Delta}^{major,init}$ for small amplitude will decrease with f shifting to the left in Fig. 18. It follows that the $\mu_{\Delta}^{major,init}(H_0^m)$ profile is expected to be of qualitatively similar shape to the $CDF(d_{nn})$ mirrored with respect to $d_{nn} = 0$, as can be observed by comparing Fig. 17 with Fig. 4 or Fig. 9 for the ex-service P9 and T22 samples respectively. In the case of excursion from major loops, f_{pin} has to take into account the effect of B_r of the sample on the domain structure. The shifting of the peak position for the μ_{Δ}^{major} profiles for excursion from the lower part of a major loop compared to the corresponding μ_{Δ}^{init} can be ascribed to a minus B_r at $H=0$ counteracting the applied field by H_c. The consistency in peak values between minor loops excursions from an initial magnetisation curve and a major loop as well as μ_r can be attributed to the same underlying microstructural feature distribution that affecting the domain processes.

Similarly, the microstructural features involved in irreversible domain processes during a minor loop can be characterised by the cross-hatched area in Fig. 18 or $\int_d^{d+\Delta d} PDF(x)\, dx$, which will not be discussed in detail in this paper as only a very small amplitude was used and hence the measured H_c^m, W_h^m and B_r^m values are more or less comparable to the scatter for H and B measurements.

6. Conclusions

Various magnetic properties measured from major loops and minor loops have been found to be sensitive to different microstructural features and have shown different behaviours in response to microstructural changes for power generation steel P9 and T22 in the different conditions (normalised, tempered and ex-service). The different sensitivities and behaviours have been

ascribed to various microstructural feature distribution affecting domain processes differently. It has been demonstrated that one can separate out the microstructural features whose pinning strength $f_{pin} \le |H_0^m|$ by applying a bias field H_0^m, at the same time, examining the features with $f_{pin} > |H_0^m|$ by looking at the incremental permeability for a small amplitude H_0^m, and/or further selecting the features that are actively impeding domain walls and eventually passed through during a minor loop by varying the minor loop amplitude H_a^m.

It was found that the initial permeability values evaluated by different techniques were in good agreement with each other including the initial permeability approximated by extrapolating the incremental permeability for unbiased minor loop measurements to zero amplitude (μ_i), the maximum incremental permeability by biased minor loop excursions from a major loop ($\mu_{\Delta_{max}}^{major}$) or an initial magnetisation curve ($\mu_{\Delta_{max}}^{init}$) and the initial permeability approximated by multi-frequency electromagnetic sensors that apply a very small magnetic field (μ_r). It was also found that the maximum incremental permeability for both unbiased minor loops with a range of amplitude and biased minor loop excursions from a major loop occur approximately at coercivity H_c for all the studied samples. This consistency in magnetic behaviours between different techniques has been attributed to similar underlying domain processes due to a same effective field ($B=0$), regardless of the externally applied field, experienced by the domain walls and hence similar microstructural features that are affecting the domain processes.

References

[1] B. Raj, V. Moorthy, T. Jayakumar, K.B.S. Rao, Assessment of microstructures and mechanical behaviour of metallic materials through non-destructive characterisation, Int. Mater. Rev. 48 (2003) 273–325, http://dx.doi.org/10.1179/095066003225010254.

[2] C.L. Davis, S.J. Dickinson, A.J. Peyton, Impedance spectroscopy for remote analysis of steel microstructures, Ironmak. Steelmak. 32 (2005) 381, http://dx.doi.org/10.1179/174328105X71254.

[3] P. Meilland, J. Kroos, O.W. Buchholtz, H.J. Hartmann, Recent developments in on-line assessment of steel strip properties, AIP Conf. Proc. 820 (1) (2006) 1780. http://dx.doi.org/10.1063/1.2184736.

[4] J. Liu, X.J. Hao, L. Zhou, M. Strangwood, C.L. Davis, A.J. Peyton, Measurement of microstructure changes in 9Cr–1Mo and 2.25Cr–1Mo steels using an electromagnetic sensor, Scr. Mater. 66 (6) (2012) 367, http://dx.doi.org/10.1016/j.scriptamat.2011.11.032.

[5] D. Jiles, Introduction to Magnetism and Magnetic Materials, 2nd edition, Chapman and Hall, London, 1998.

[6] J. Liu, M. Strangwood, C.L. Davis, A.J. Peyton, Magnetic evaluation of microstructure changes in 9Cr–1Mo and 2.25Cr–1Mo steels using electromagnetic sensors, Metall. Mater. Trans. A 44 (13) (2013) 5897–5909, http://dx.doi.org/10.1007/s11661-013-1938-x.

[7] S. Takahashi, S. Kobayashi, H. Kikuchi, Y. Kamada, Relationship between mechanical and magnetic properties in cold rolled low carbon steel, J. Appl. Phys. 100 (11) (2006) 113908, http://dx.doi.org/10.1063/1.2401048.

[8] S. Takahashi, S. Kobayashi, H. Kikuchi, Y. Kamada, K. Ara, Analysis of minor hysteresis loops of cold rolled low carbon steel, IEEE Trans. Magn. 42 (11) (2006) 3782–3784, http://dx.doi.org/10.1109/TMAG.2006.879147.

[9] S. Kobayashi, M. Tanaka, T. Kimura, Y. Kamada, H. Kikuchi, S. Takahashi, T. Ohtani, Changes of magnetic minor hysteresis loops during creep in Cr–Mo–V ferritic steel, J. Electr. Eng. 59 (7/s) (2008) 29–32.

[10] L. Vandenbossche, L. Dupré, J. Melkebeek, Evaluating material degradation by the inspection of minor loop magnetic behavior using the moving Preisach formalism, J. Appl. Phys. 99 (8) (2006) 08D907-1–08D907-6, http://dx.doi.org/10.1063/1.2170960.

[11] H.C. Furtado, L.H. de Almeida, I. Le May, Precipitation in 9Cr–1Mo steel after creep deformation, Mater. Charact. 58 (1) (2007) 72–77, http://dx.doi.org/10.1016/j.matchar.2006.04.001.

[12] ASTM, Standard Specification for Seamless Ferritic Alloy-Steel Pipe for High-Temperature Service, A335/A335M-09A, 2009. http://dx.doi.org/10.1520/A0335_A0335M-10.

[13] ASTM, Standard Specification for Seamless Ferritic and Austenitic Alloy-Steel boiler, Superheater, and Heat-Exchanger Tubes, A213/A213M-09B, 2009. http://dx.doi.org/10.1520/A0213_A0213M-09b.

[14] S. Saroja, M. Vijayalakshmi, V.S. Raghunathan, Effect of prolonged exposures of 9Cr–1Mo–0.07C steel to elevated temperatures, Mater. Trans. JIM 34 (10) (1993) 901–906, http://dx.doi.org/10.2320/matertrans1989.34.901.

[15] J.R. Yang, C.Y. Huang, C.N. Yang, J.L. Horng, Microstructural examination of 2.25Cr–1Mo steel steam pipes after extended service, Mater. Charact. 30 (2) (1993) 75–88, http://dx.doi.org/10.1016/1044-5803(93)90011-j.

[16] B. Arivazhagan, R. Prabhu, S. Albert, M. Kamaraj, S. Sundaresan, Microstructure and mechanical properties of 9Cr–1Mo steel weld fusion zones as a function of weld metal composition, J. Mater. Eng. Perform. 18 (8) (2009) 999–1004, http://dx.doi.org/10.1007/s11665-008-9349-7.

[17] G. Sangdahl, M. Semchyshen, Application of 2.25Cr–1Mo Steel for Thick-Wall Pressure Vessels, ASTM, 1982. http://dx.doi.org/10.1520/STP755-EB.

[18] B.L. Bramfitt, A.O. Benscoter, Metallographer's Guide Practice and Procedures for Irons and Steels, ASM International, Materials Park, OH, 2001.

[19] H. Ghassemi-Armaki, R.P. Chen, K. Maruyama, M. Yoshizawa, M. Igarashi, Static recovery of tempered lath martensite microstructures during long-term aging in 9–12% Cr heat resistant steels, Mater. Lett. 63 (28) (2009) 2423–2425, http://dx.doi.org/10.1016/j.matlet.2009.08.024.

[20] P. Ennis, A. Czyrska-Filemonowicz, Recent advances in creep-resistant steels for power plant applications, Sadhana—Acad. Proc. Eng. Sci. 28 (3) (2003) 709–730, http://dx.doi.org/10.1007/BF02706455.

[21] A. Zielinska-Lipiec, A. Czyrska-Filemonowicz, P.J. Ennis, O. Wachter, The influence of heat treatments on the microstructure of 9% chromium steels containing tungsten, J. Mater. Process. Technol. 64 (1–3) (1997) 397–405, http://dx.doi.org/10.1016/s0924-0136(96)02591-5.

[22] J. Pesicka, R. Kuzel, A. Dronhofer, G. Eggeler, The evolution of dislocation density during heat treatment and creep of tempered martensite ferritic steels, Acta Mater. 51 (16) (2003) 4847–4862, http://dx.doi.org/10.1016/s1359-6454(03)00324-0.

[23] J. Šternberk, E. Kratochvílová, A. Gemperle, V. Faja, V. Walder, Dependence of characteristics of hysteresis loops on dislocation densities for low-alloy Cr–Mo steel, Czech. J. Phys. 35 (11) (1985) 1259–1266, http://dx.doi.org/10.1007/bf01597011.

[24] J. Šternberk, E. Kratochvílová, J. Hřebík, A. Gemperle, Coercivity and microstructure of low-alloy Cr–Mo steel, Phys. Status Solidi A 79 (2) (1983) 523–529, http://dx.doi.org/10.1002/pssa.2210790225.

[25] M. Yoshino, Y. Mishima, Y. Toda, H. Kushima, K. Sawada, K. Kimura, Influence of normalizing heat treatment on precipitation behaviour in modified 9Cr1Mo steel, Mater. High Temp. 25 (3) (2008) 149–158, http://dx.doi.org/10.3184/096034008x356349.

[26] G. Fillion, M. Lord, J. Bussière, Inference of hardness from magnetic measurements in pearlitic steels, in: D. Thompson, D. Chimenti (Eds.), Review of Progress in Quantitative Nondestructive Evaluation, Springer, USA, 1990, pp. 1887–1893, http://dx.doi.org/10.1007/978-1-4684-5772-8_242.

[27] B.K. Tanner, J.A. Szpunar, S.N.M. Willcock, L.L. Morgan, P.A. Mundell, Magnetic and metallurgical properties of high-tensile steels, J. Mater. Sci. 23 (12) (1988) 4534–4540, http://dx.doi.org/10.1007/bf00551956.

[28] H. Danan, A. Herr, A.J.P. Meyer, New determinations of the saturation magnetization of nickel and iron, J. Appl. Phys. 39 (2) (1968) 669–670, http://dx.doi.org/10.1063/1.2163571.

[29] M. Cadeville, E. Daniel, Sur la structure électronique de quelques borures d'éléments de transition, J. Phys. Paris 27 (7–8) (1966) 449–457, http://dx.doi.org/10.1051/jphys:01966002707-8044900.

[30] J.B. Goodenough, A theory of domain creation and coercive force in polycrystalline ferromagnetics, Phys. Rev. 95 (4) (1954) 917–932, http://dx.doi.org/10.1103/PhysRev.95.917.

[31] L. Neel, Cah. Phys. 25 (1944) 21–44.

[32] Z.J. Chen, D.C. Jiles, Modelling of reversible domain wall motion under the action of magnetic field and localized defects, IEEE Trans. Magn. 29 (6) (1993) 2554–2556, http://dx.doi.org/10.1109/INTMAG.1993.642509.